Supporting Information for

Thermally Stable N_2-intercalated WO_3 Photoanodes for Water Oxidation

Qixi Mi,[1] Yuan Ping,[2] Yan Li,[3] Bingfei Cao,[4] Bruce S. Brunschwig,[1] Peter G. Khalifah,[4,5,] Giulia A. Galli,[2,]* Harry B. Gray[1,]* and Nathan S. Lewis[1,]**

[1]Beckman Institute and Kavli Nanoscience Institute, Division of Chemistry and Chemical Engineering, California Institute of Technology, M/C 127-72, 1200 E. California Blvd., Pasadena, CA 91125

[2]Department of Chemistry, University of California, One Shields Ave., Davis, CA 95616

[3]Computational Science Center, [4]Department of Chemistry, Brookhaven National Laboratory, Upton, New York, NY 11973

[5]Department of Chemistry, Stony Brook University, Stony Brook, New York, NY 11974.

Synthesis of Ammonium-^{15}N paratungstate tetrahydrate

$$12\ H_2WO_4 + 10\ {}^{15}NH_3{\cdot}H_2O \xrightarrow{80\ ^\circ C} ({}^{15}NH_4)_{10}[H_2W_{12}O_{42}]{\cdot}4H_2O$$

In a 20-ml vial, 1.00 g (4.00 mmol) of tungstic acid (Alfa Aesar 82118) was suspended in 5.0 ml water at 80 °C under rigorous stirring. After dropwise addition of 3.00 ml (9.9 mmol) of $^{15}NH_3{\cdot}H_2O$ (Cambridge Isotope Laboratories NLM-1320, 3.3 N, 98+% ^{15}N), the tungstic acid dissolved within several minutes, giving a colorless, clear or slightly hazy solution.

The reaction mixture was capped and allowed to stand at 80 °C for 30 min, before slowly evaporating to dryness. Colorless granular crystals, 1.01 g (0.321 mmol, 96% based on W), appeared on the bottom as well as on the walls of the vial. The crude crystals were washed with a small amount of water, transferred to a Büchner funnel, filtered, and dried in air to yield 0.895 g (0.285 mmol, 86%) of colorless crystals. Powder X-ray diffraction (Cu *K*α, °): 8.78, 10.57, 12.17; Reference (Inorganic Crystal Structure Database 158755): 8.72, 10.50, 12.10.

Refinement of x-ray structures

Based on the large width of the 112_{cubic} class of reflections relative to the 100_{cubic} reflections, it was determined that the symmetry of these compounds was monoclinic or lower. Due to the broadened peaks, a direct inspection of X-ray patterns was not sufficient to distinguish between the ε (low-temperature monoclinic), δ (low-temperature triclinic), and γ (room temperature monoclinic) polymorphs of WO_3. These three structures only differ in slight variations of their octahedral tilts and in their vectors of displacement of W from the center of WO_6 octahedra, and as a result have strongly overlapping reflection positions (all cell angles deviate by less than 2° from those of orthorhombic β-WO_3, and the structure factors of related reflections are barely affected by the changes in space group symmetry). A close investigation of X-ray diffraction peak profiles revealed that the peaks of all samples that were investigated could not be precisely fit with a single phase with pseudo-Voigt peaks even after accounting for well-understood instrumental broadening effects through the fundamental parameters approach of TOPAS. This indicates the presence of either a minor fraction (<25%) of a structurally-related second phase (i.e. a WO_3 polymorph with a different symmetry and overlapping peaks) or the presence of asymmetric strain (non-Gaussian and non-Lorentzian) within the sample (as could conceivably occur if the N_2 contents depended on the depth from the sample surfaces).

The pseudosymmetry of the lattice negated the utility of model-independent fitting techniques (Le Bail, Pawley) in obtaining accurate lattice parameters. Instead, Rietveld refinements were carried out to follow lattice parameter changes within the restrictions of a structural model of γ-WO_3. The positions of W atoms were allowed to freely refine, while O atoms were fixed at the fractional coordinates determined previously. Thermal parameters (ADPs) were fixed at chemically plausible values of B = 0.5 for W and B = 1.0 for O. Peak broadening effects were modeled using only strain effects, because minor size broadening effects could not be effectively deconvoluted. For the final reported lattice parameters, X-ray diffraction data were recollected with an internal standard of LaB_6 whose lattice parameters were fixed to the values determined by the supplier (Gem Dugout) in a simultaneous refinement of all four patterns. The robustness of the lattice parameter results was verified by comparative studies with data collected on two other instruments (P'Analytical X-ray diffractometer with a Cu $K\alpha$ source at California Institute of Technology and POWGEN3 time-of-flight neutron diffractometer at the Spallation Neutron

Source, Oak Ridge, Tennessee), which all showed the same trends in the dependence of lattice parameters on the sample preparation method.

Supporting data

Table S1. Stokes shifts (in cm^{-1}) of N_2 in various environments. Differences between computed and measured frequencies are partly due to the use of the harmonic approximation in the calculations.

Method	Condition	$\nu(^{14}N_2)$	$\nu(^{15}N_2)$
Raman Spectroscopy	Gas phase[a]	2330	2252
	N_2 clathrate hydrate at 0.5 GPa[b]	2324	
	N_2 in porous SiO_2[c]	2321	
	N_2 in 4A molecular sieves[d]	2324	
	N_2 in metal–organic frameworks[e]	2326–2327	
	$0.034N_2{\cdot}WO_3$ annealed at 750 °C	2327	2249
	$0.039N_2{\cdot}WO_3$ annealed at 550 °C	2326, 2338	2248, 2260
	$0.039N_2{\cdot}WO_3$ annealed at 420 °C	2326, 2339	2248, ~2258
Computation	Gas phase	2383	
	$N_2{\cdot}8WO_3$	2373, 2391	

[a] References[1,2]; [b] References[3,4]; [c] Reference[5]; [d] Reference[6]; [e] Reference[7].

Table S2. Equilibrium lattice constants of monoclinic WO_3 at room temperature (Figure 1A).

	a (Å)	*b* (Å)	*c* (Å)	*β* (°)
Experimental	7.31	7.53	7.69	90.78
Calculated[a]	7.35	7.45	7.66	90.60

[a] Calculations were performed using density functional theory (DFT), the local density approximation (LDA), and norm-conserving Hartwigsen–Goedecker–Hutter (HGH) type pseudopotentials,[8] including semi-core (5*s*, 5*p*) electrons. A kinetic energy cutoff of 120 Ry, and (3×3×3) Monkhorst–Pack *k*-point grids were used in the calculations. Both internal geometry and cell size were fully optimized.

Table S3. Lattice parameters obtained from Rietveld refinements of the X-ray diffraction patterns of $xN_2{\cdot}WO_3$.[a]

	Pure monoclinic WO_3	$0.034N_2{\cdot}WO_3$ annealed at 750 °C	$0.039N_2{\cdot}WO_3$ annealed at 550 °C	$0.039N_2{\cdot}WO_3$ annealed at 420 °C
a (Å)	7.3082(3)	7.3235(3)	7.3442(5)	7.3571(6)
b (Å)	7.5305(3)	7.5219(3)	7.5133(5)	7.5046(6)
c (Å)	7.6899(4)	7.6954(3)	7.6900(5)	7.6808(7)
β (°)	90.785(7)	90.549(8)	90.46(2)	90.56 (2)
V (Å^3)	423.17(3)	423.90(3)	424.32(5)	424.05(6)
S_L (%)	0.34(2)	0.75(2)	0.63(3)	0.67(4)
S_G (%)	0.01(13)	0.34(3)	1.25(2)	1.13(4)
e_0 (%)	0.085(4)	0.223(6)	0.406(9)	0.38(1)
R_{exp} (%)	2.19	2.15	2.31	2.31
R_{wp} (%)	17.84	8.37	8.32	8.47
R_p (%)	13.02	6.36	5.98	6.44
GOF	8.15	3.89	3.56	3.67

[a] LaB_6 was used as an internal standard. Parameters: V, cell volume; S_L, Lorentzian-type strain component; S_G, Gaussian-type strain component; e_0, mean strain; R_{exp}, statistically expected R value; R_{wp}, weighted profile R value; R_p, profile R value; GOF, goodness of fit.

Table S4. Calculated band gaps (in eV) of pure monoclinic WO_3 and $N_2{\cdot}8WO_3$ at zero temperature.[a]

Levels of theory	Cell parameters	LDA	LDA	LDA
	Internal coordinates	LDA	LDA	PBE0
	Band gap	LDA	PBE0	PBE0
Calculated band gaps	Pure WO_3 (B → Γ)	1.30	3.28	3.08
	$N_2{\cdot}8WO_3$ (Y → Γ)	1.13	3.15	2.93

[a] PBE0 calculations were carried out with the Qbox code.[9] The difference between direct and indirect band gap is less than 0.01 eV in all calculations. Note the same trend, i.e., band gap reduction from pure monoclinic WO_3 to $N_2{\cdot}8WO_3$, is obtained with all functionals.

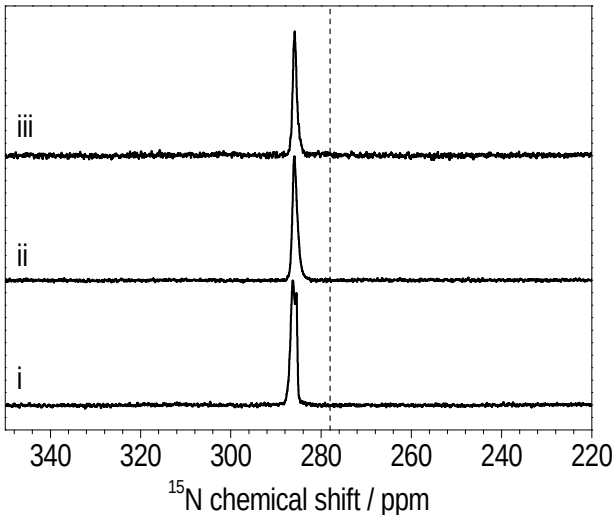

Figure S1. ^{15}N solid-state NMR spectra of (i) $0.034^{15}N_2 \cdot WO_3$ annealed at 750 °C, (ii) $0.039^{15}N_2 \cdot WO_3$ annealed at 550 °C, and (iii) $0.039^{15}N_2 \cdot WO_3$ annealed at 420 °C. The dashed vertical line denotes the chemical shift (278 ppm[10]) of $^{15}N_2$(g). Chemical shifts are referenced to $^{15}NH_4^+$.

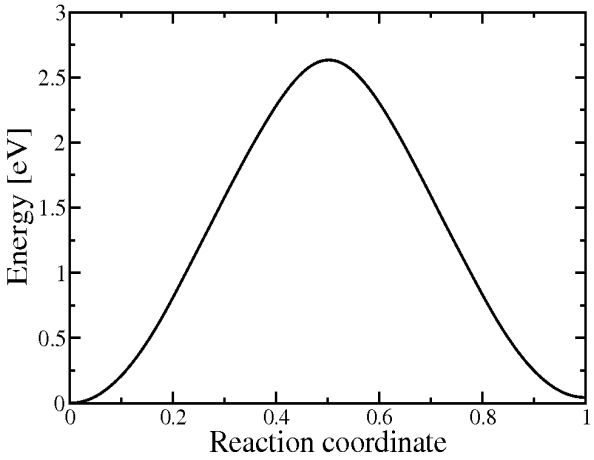

Figure S2. Nudged elastic band[11] calculation of the energy barrier for an N_2 molecule diffusing across two neighboring lattice cells. Twenty points on the reaction path are sufficient are sufficient to reach convergence of activation energies to 0.01 eV. Calculations were carried out with the QUANTUM ESPRESSO package.[12]

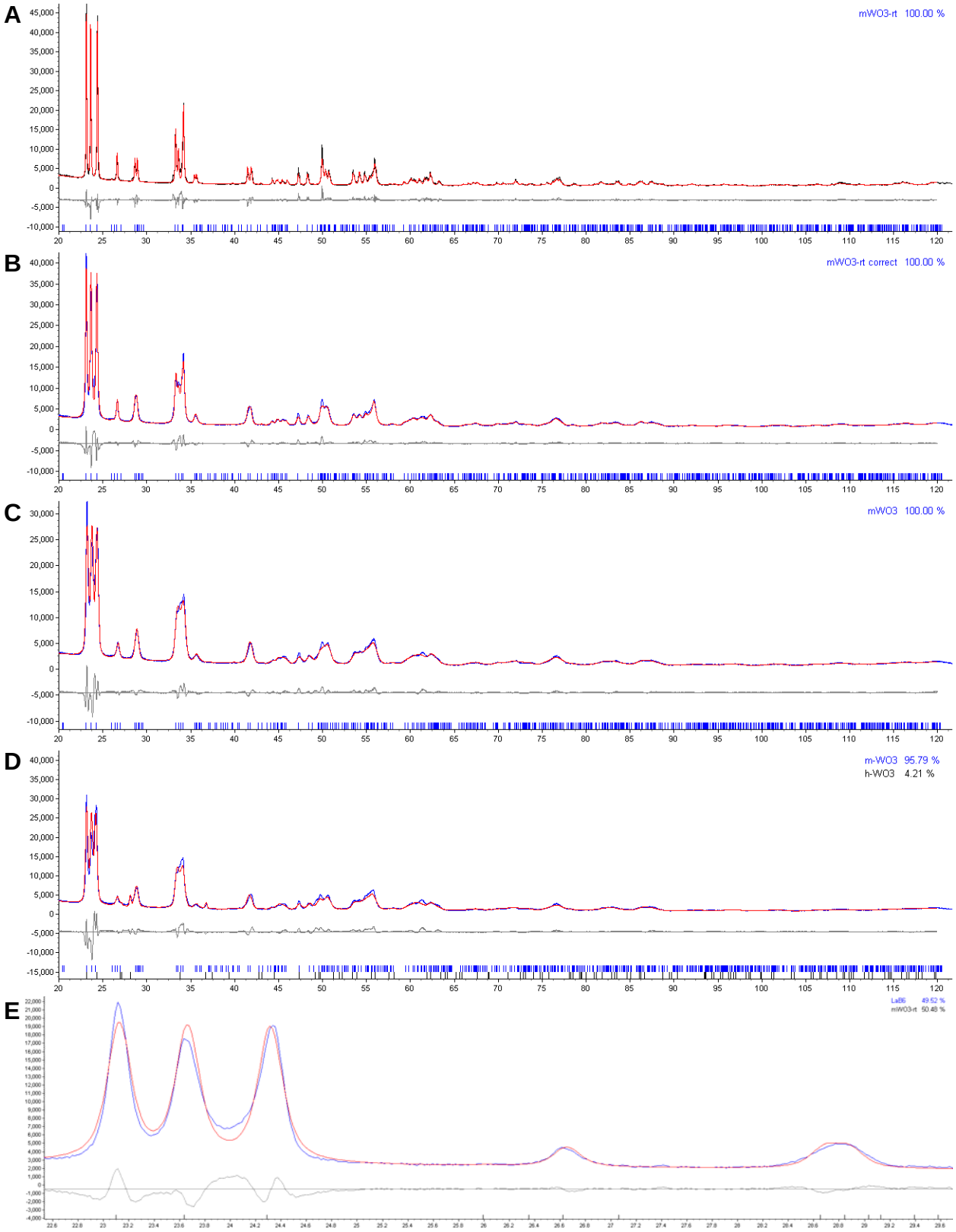

Figure S3. Measured (blue), Rietveld-modeled (red) X-ray diffraction patterns, and the differ-

ences (gray) of (**A**) pure monoclinic WO_3; (**B**) $0.034N_2{\cdot}WO_3$ annealed at 750 °C; (**C**) $0.039N_2{\cdot}WO_3$ annealed at 550 °C; and (**D**) $0.039N_2{\cdot}WO_3$ annealed at 420 °C. Samples were identical to those used for lattice parameter analysis with a LaB_6 internal standard. Panel (**E**) is a detail of panel (**B**) over the range $2\theta = 22°–30°$, which highlights the challenges in fitting the 002, 020, and 200 peaks (22°–24°), and the broadened 112-type peak at $2\theta \approx 29°$, which indicated a symmetry lower than orthorhombic.

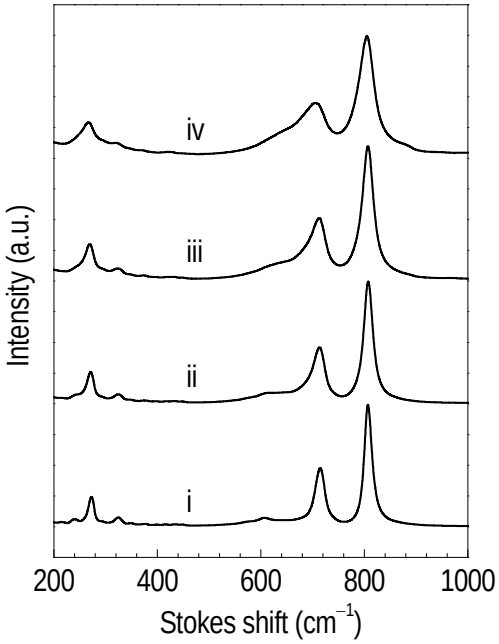

Figure S4. Room-temperature Raman spectra in the range of 200–1000 cm^{-1} for (i) pure monoclinic WO_3, (ii) $0.034N_2{\cdot}WO_3$ annealed at 750 °C, (iii) $0.039N_2{\cdot}WO_3$ annealed at 550 °C, and (iv) $0.039N_2{\cdot}WO_3$ annealed at 420 °C. A.u.: arbitrary units.

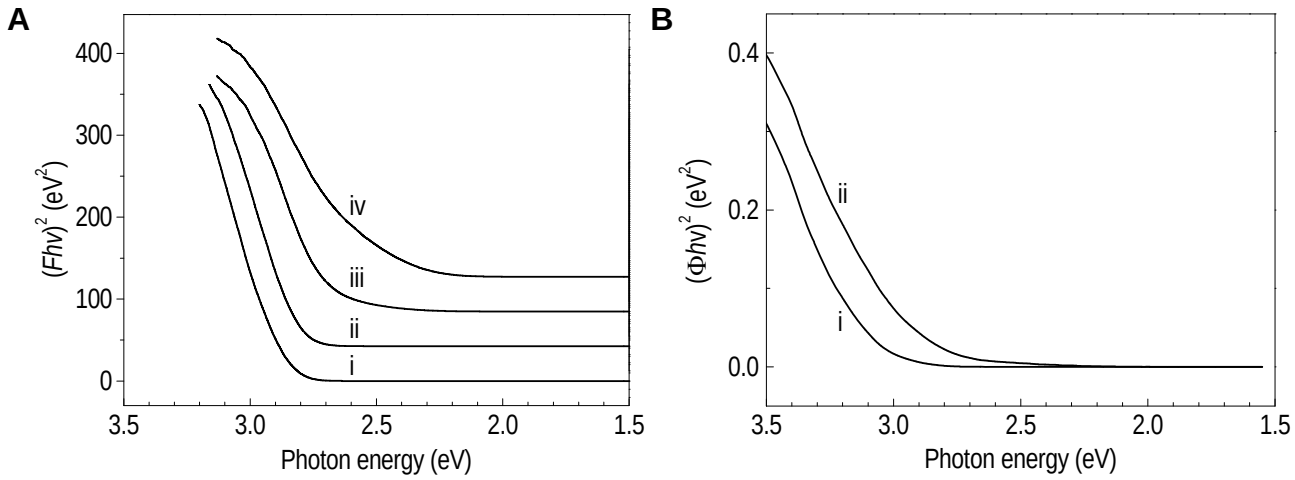

Figure S5. (**A**) Diffuse reflectance spectra (vertically offset for clarity) of (i) pure monoclinic WO_3; (ii) $0.034N_2{\cdot}WO_3$ annealed at 750 °C; (iii) $0.039N_2{\cdot}WO_3$ annealed at 550 °C; and (iv) $0.039N_2{\cdot}WO_3$ annealed at 420 °C. (**B**) Spectral response data for (i) pure monoclinic WO_3 and (ii) $0.039N_2{\cdot}WO_3$ annealed at 420 °C during the potentiostatic photoanodic oxidation of 1.0 M HCl(aq) to Cl_2(g). Note that those plots as $(Fh\nu)^2$ or $(\Phi h\nu)^2$ vs. $h\nu$ do not produce a well-defined region for extrapolation, which suggests an indirect E_g for these materials.

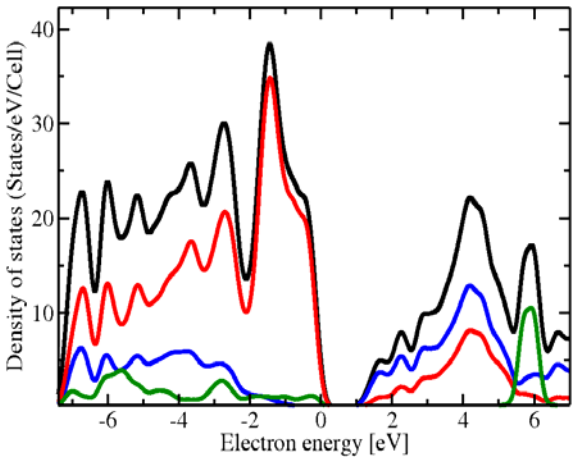

Figure S6. Projected density of states (DOS) of monoclinic $2N_2{\cdot}8WO_3$. The blue, red, and green curves represent the contributions from W 5*d*, O 2*p*, and N 2*p* atomic orbitals, respectively, to the total DOS (black).

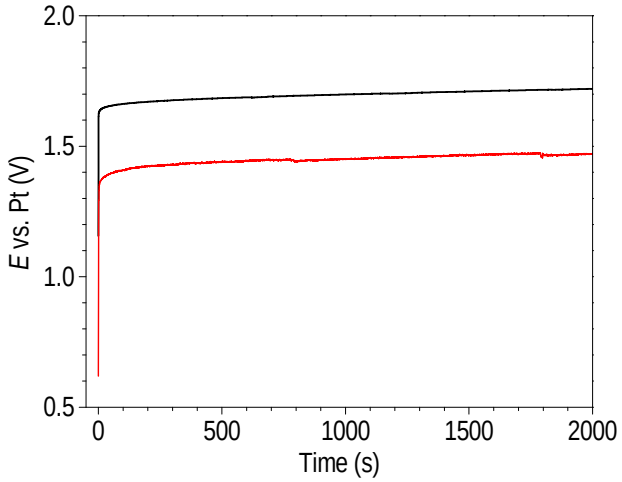

Figure S7. Cell voltages of an illuminated $0.039N_2 \cdot WO_3$ photoanode (red) and of a dark RuO_2 electrode (black) during galvanostatic (photo)electrolysis (0.50 mA, 2000 s) of 1.0 M $HClO_4$(aq), using a Pt counter electrode and no reference electrode.

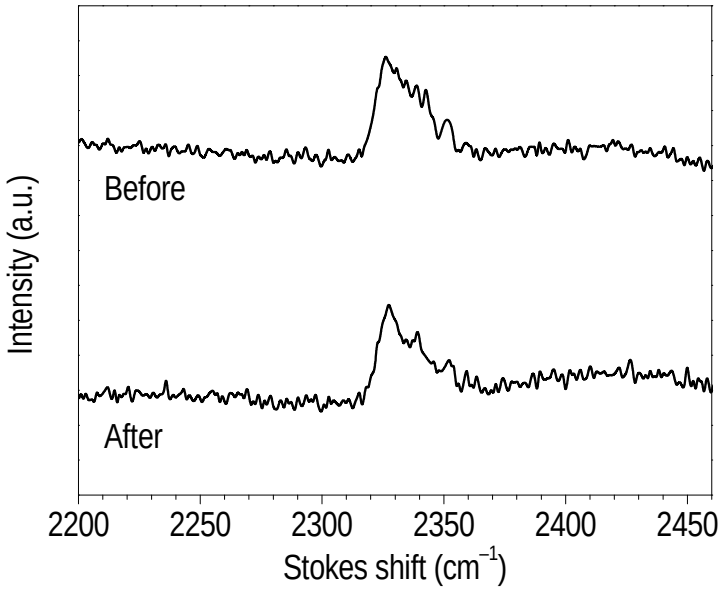

Figure S8. Raman spectra of a $0.039N_2 \cdot WO_3$ photoanode before and after photoelectrolysis of 1.0 M $HClO_4$(aq) at 0.50 mA for 2000 s.

References

(1) Bendtsen, J.; Rasmussen, F. *J. Raman Spectrosc.* **2000**, *31*, 433–438.

(2) Bendtsen, J. *J. Raman Spectrosc.* **2001**, *32*, 989–995.

(3) van Hinsberg, M. G. E.; Scheerboom, M. I. M.; Schouten, J. A. *J. Chem. Phys.* **1993**, *99*, 752–754.

(4) Sasaki, S.; Hori, S.; Kume, T.; Shimizu, H. *J. Chem. Phys.* **2003**, *118*, 7892–7897.

(5) Kolesov, B. A.; Geiger, C. A. *Am. Mineral.* **2003**, *88*, 1364–1368.

(6) Saperstein, D. D.; Rein, A. J. *J. Phys. Chem.* **1977**, *81*, 2134–2135.

(7) Siberio-Perez, D. Y.; Wong-Foy, A. G.; Yaghi, O. M.; Matzger, A. J. *Chem. Mater.* **2007**, *19*, 3681–3685.

(8) Hartwigsen, C.; Goedecker, S.; Hutter, J. *Phys. Rev. B* **1998**, *58*, 3641–3662.

(9) http://eslab.ucdavis.edu/software/qbox.

(10) Jameson, C. J.; Jameson, A. K.; Oppusunggu, D.; Wille, S.; Burrell, P. M.; Mason, J. *J. Chem. Phys.* **1981**, *74*, 81–88.

(11) Henkelman, G.; Uberuaga, B. P.; Jónsson, H. *J. Chem. Phys.* **2000**, *113*, 9901–9904.

(12) Giannozzi, P.; Baroni, S.; Bonini, N.; Calandra, M.; Car, R.; Cavazzoni, C.; Ceresoli, D.; Chiarotti, G. L.; Cococcioni, M.; Dabo, I.; Dal Corso, A.; de Gironcoli, S.; Fabris, S.; Fratesi, G.; Gebauer, R.; Gerstmann, U.; Gougoussis, C.; Kokalj, A.; Lazzeri, M.; Martin-Samos, L.; Marzari, N.; Mauri, F.; Mazzarello, R.; Paolini, S.; Pasquarello, A.; Paulatto, L.; Sbraccia, C.; Scandolo, S.; Sclauzero, G.; Seitsonen, A. P.; Smogunov, A.; Umari, P.; Wentzcovitch, R. M. *J. Phys. Condens. Matter* **2009**, *21*, 395502.